6-1-2005

Modelling continuum optical and ultraviolet polarization of active galactic nuclei

René W. Goosmann
Observatoire de Paris, goosmann@astro.u-strasbg.fr

C. Martin Gaskell
University of Nebraska-Lincoln, mgaskell@ucsc.edu

Astronomy & Astrophysics manuscript no. goosmann-gaskell July 5, 2005
(DOI: will be inserted by hand later)

Modelling continuum optical and ultraviolet polarization of active galactic nuclei

René W. Goosmann[1] and C. Martin Gaskell[2]

[1] Observatoire de Paris - Meudon, 5, place Jules Janssen, 92190 Meudon, France
e-mail: rene.goosmann@obspm.fr
[2] Department of Physics & Astronomy, University of Nebraska Lincoln, NE 68588-0111, USA
e-mail: mgaskell1@unl.edu

Received June 2005; accepted ___

Abstract. We present results from a new Monte Carlo radiative transfer computer code, *STOKES*, developed to model polarization induced by scattering off free electrons and dust grains. *STOKES* is freely available on the web and can be used to model scattering in a wide variety of astrophysical situations.
For edge-on (type-2) viewing positions, the polarization produced by a dusty torus alone is largely wavelength-independent. This is because the torus is optically thick and the change in albedo with wavelength is slight. Wavelength-independent polarization therefore does not necessarily imply electron scattering. We are able to fully explain wavelength independent type-2 polarization without the need to invoke electron scattering cones and consider the dusty torus to be main origin of the polarization in type-2 Seyferts.
Polarization perpendicular to the axis of symmetry in type-2 AGNs requires torus half-opening angles of $<\sim 60°$. The degree of polarization is a strong function of the half-opening angle. The high polarizations observed in type-2 AGNs imply half-opening angles $\leq 30°$.
The polarization parallel to the axis of symmetry seen in many type-1 (face-on) AGNs cannot be explained by scattering from a torus alone, or by a torus plus scattering cones. For type-1 objects, the torus gives negligible polarization and electron cones give the wrong angle of polarization. The parallel polarization must arise from a flattened electron-scattering distribution inside the torus. We demonstrate how both the accretion disc itself, and a flattened nearby electron-scattering region can produce the required degree of polarization. We show how the expected polarization varies with the flattening of the regions and source coverage. The dominant parameter influencing the parallel polarization is the electron-scattering optical depth. For a highly ionized emitting and scattering accretion disk an optical depth of only a few tenths is sufficient to produce the observed polarization.

Key words. Galaxies: active – Polarization – Radiative transfer – Scattering – Dust

1. Introduction

Polarimetry was introduced to astronomy over a half century ago (Hall 1949, Hiltner 1949). Since then, the significance of polarimetry in astronomy has been steadily rising. Since angle-dependent scattering is one of the major causes of polarization, polarization can provide valuable information about the geometry of astronomical sources. The techniques of polarimetry have been combined with the techniques of spectroscopy to give spectropolarimetry which enables investigations of the detailed wavelength-dependence of polarization. When emission lines show structure in polarized flux it is also possible to draw conclusions about the kinematics of scattering material.

The field of active galactic nucleus (AGN) research is faced with the problem that the dimensions of the innermost regions of AGNs subtend angles that are far too small to be resolved in the optical with current technology. It has long been known that the light of AGNs is polarized over a broad wavelength range, and spectropolarimetry is a helpful instrument in constraining the structure of AGNs.

Rowan-Robinson 1997 suggested that AGNs were surrounded by a dusty torus and in the same paper he gives a suggestion by M. V. Penston that Seyfert 2 galaxies are seen near to edge-on so that the active nucleus is obscured by the torus. Support for the picture came from the important discovery by Keel (1980) that Seyfert 1 galaxies (active galaxies showing a broad line region; BLR) are preferentially face-on and this led to further confirmation of the importance of orientation effects (Lawrence & Elvis 1982; De Zotti & Gaskell 1985). The dusty-torus model has become the standard unified model (see Antonucci 2002). In this paper we will refer to AGNs seen near to face-on as "type-1 AGNs" and to objects seen near to edge-on as "type-2" AGNs. In type-1 AGNs the central energy source and its surroundings (e.g., the BLR) can

Send offprint requests to: René W. Goosmann

be seen; in type-2 AGNs the torus blocks our direct view of the inner regions.

Antonucci & Miller (1985) made the key discovery that the polarized flux spectrum can offer a periscopic view for type-2 AGNs. Their detection of a hidden broad-line region in the type-2 AGN NGC 1068 was of great importance for AGN research since it provided strong support for the unified theories of AGN activity. More hidden type-1 nuclei have subsequently been found by analysis of their polarized flux spectrum (see e.g., Miller & Goodrich, 1990; Tran, Miller, & Kay, 1992; Hines & Wills, 1993; Kay, 1994; Heisler, Lumsden, & Bailey,1997; Tran, 2001; Smith et al., 2004). Similar work on the radio galaxy 3C 321 was done by Hurt et al. (1999) and Tran et al. (1999) could identify an active nucleus inside an ultra-luminous infra-red galaxy by using spectropolarimetry.

The new generation of large telescopes and improved measuring techniques are delivering detailed spectropolarimetry of emission lines (see, for example, the spectropolarimetry of the Seyfert 1.5 galaxy NGC 4151 presented by Martel 1998, and the atlas of spectropolarimetry of Seyfert galaxies presented by Smith et al. 2002). Examination of such spectropolarimetric data promises to reveal valuable information about the geometry of the BLR (Smith et al. 2005). Similarly, spectropolarimetry of quasar absorption lines should help constraining the geometry of broad absorption line QSOs (Goodrich & Miller 1995, Cohen et al. 1995, Hines & Wills 1995).

In order to obtain a detailed understanding of observed polarization, and of the underlying geometry, theoretical modelling is necessary. Analytical approaches to radiative transfer that have been carried out so far are generally limited to the consideration of single-scattering models. Computer simulations are needed to investigate multiple-scatterings. In this paper we describe *STOKES*, a new general-purpose Monte Carlo code for modelling wavelength-dependent polarization in a wide-variety of scenarios, and present some results of our study of AGN polarization.

Most AGNs investigated reveal amounts of continuum polarization between 0% and 20%. An interesting behaviour has been observed for the polarization position angle: for many (but not all) type-1 objects it favors a direction *parallel* to the symmetry axis defined by the radio jets, if apparent, or by the weaker radio structure found Seyfert galaxies. On the other hand, for type-2 objects the position angle tends to be directed *perpendicular* to the radio axis (Antonucci 1982, 1983).

In this paper we use *STOKES* to demonstrate a likely cause of this dichotomy. In section 2 we summarize some results of previous AGN polarization modelling. In section 3 we describe *STOKES*, in section 4 we describe the application of *STOKES* to the modelling from AGN tori, and in section 5 we investigate how the parallel polarization seen in type-1 objects results from the scattering from various possible flattened, electron-scattering discs. Our results are discussed in section 6 and we summarize our conclusions in section 7.

2. Results of Previous Modelling

Efstathiou & Rowan-Robinson (1995) modelled radiative transfer in a dusty torus, but did not consider polarization. Young et al. (1996, 1995), Packham (1997), and Young (2000) developed an analytical radiative transfer model for polarization. Their model was based on the unified AGN model. Extended emission regions can be defined and scattering processes as well as dichroic absorption are considered. The modelled geometries include toroidal and conical regions of dust and free electrons. For moving scattering clouds a Doppler shift of the scattered radiation is included. The model is fairly effective in reproducing spectropolarimetric data of NGC 1068 as well as giving the variations across the Hα line and time-dependent polarization in Mrk 509. Their model requires user-definition of many free parameters and multiple scattering is not considered.

Gordon et al. (2001) and Misselt et al.(2001) applied their code DIRTY to modelling polarization of two highly-polarized IRAS-objects: IRAS 13349+2438, and IRAS 14026+4341 (Hines et al. 2001). In the model space of DIRTY, single photons were allowed to escape from a point source into two polar cones. Dust was arranged round the source in a spherical geometry. The photons undergo scattering, absorption and re-emission processes on their way through the dust. Two types of dust were used: Milky Way (MW) dust and Small Magellanic Cloud (SMC) bar dust. The grain size distributions where fit to known MW and SMC extinction curves. Photons that escape from the model region are detected and registered according to their direction of flight. For certain viewing angles and optical depths of the scattering material the observed spectral polarization shape of both objects could be qualitatively verified.

Wolf & Henning (1999) defined both double-conical distributions of free electrons and dust as well as dusty tori in their model space. They found that the observed wavelength dependence of polarization in some AGN (i.e., polarization decreasing with wavelength) can be modelled by dust scattering inside the cones. The presence of additional free electrons in the conical regions increases the absolute amount of polarization.

An important element in Wolf & Henning's work is that multiple scattering is considered accurately by including dependence of scattering angle and polarization of a scattered photon on the incident Stokes vector. It turned out that multiple scattering became important for optical depths $\gtrsim 0.1$. Two different dust size distributions were examined: Galactic dust and a distribution favoring larger grains - no relevant differences in the polarization properties were seen. Since the code allows polarization imaging it was possible to create resolved polarization maps of simulated AGN geometries.

Kartje (1995) developed a Monte Carlo Code and investigated quasar schemes with either a torus geometry or conical stratified winds along the polar axis. In addition to polarization by scattering he also considered polarization by dichroic extinction due to magnetically -aligned dust grains. For a simple unified torus model he found that the dominant parameter of the polarization, P, is the torus half-opening angle: for type-2-objects one can find significant polarization up to 30% with a position angle directed perpendicular to the axis of symmetry; for type-1-objects P is negligible. Kartje obtained a striking result when he investigated conical stratified-wind regions containing ionized material closer to the central source and dust farther out: the amount of polarization ranges between 0% and

13%, matching the observed values, and the direction of the ***E***-vector depends on viewing angle in a manner that agrees with the above-mentioned type-1/type-2-dichotomy. The polarization percentage can be increased if there is magnetic alignment of dust grains, but the the general dependence of P on the viewing angle seems to be a geometrical effect.

Another Monte-Carlo polarization code was written by Watanabe et al. (2003). It was applied to modeling of optical and near-infrared spectrapolarimetric data of the type-2 Seyfert galaxies Mrk 463E, Mrk1210, NGC 1068, and NGC 4388. The code contains electron and dust scattering routines quite similar to those used by Wolf & Henning (1999). It considers multiple scattering and dichroic absorption in dusty tori, spheres as well as electron and dust scattering in double-conical regions. Absorption and scattering properties of the dust are carefully calculated by Mie theory. Watanabe et al. (2003) examine wavelength-dependent polarization properties for different geometries over a broad-wavelength range and give constrains about possible scattering components within the objects they observed. They conclude that a combination of dust and electron scattering in polar regions can reproduce the optical polarization properties observed in Mrk 463E and Mrk1210. The slope of optical polarization NGC 1068 is almost flat favoring electron scattering as the dominant polarizing process. For the near-infrared range polarization of these objects can be modelled by dichroic absorption of aligned dust grains in a torus. However, scattering off Galactic dust in a torus cannot simultaneously reproduce near-infrared polarization and the total flux. Watanabe et al. (2003) hence suggest that the grains size composition of AGNs might be different from our Galaxy.

3. STOKES - an overview

The computer program *STOKES* performs simulations of radiative transfer, including the treatment of polarization, for AGNs and related objects . The code is based on the Monte Carlo method and follows single photons from their creation inside the source region through various scattering processes until they become absorbed or manage to escape from the model region and are observed (Fig. 1). The polarization properties of the model photons are given by their stored Stokes vectors.

Photons are created inside the source regions, which can be realized by different geometries. The program allows input of complicated continuum and line emitting region geometries. The continuum radiation is defined by the index α of an $F_\nu \propto \nu^{-\alpha}$ power law. The Stokes vectors of the photons are initially set to the values of completely unpolarized light.

Around the source, various geometries of scattering mirrors can be arranged. The program offers toroidal, cylindrical, spherical or conical shapes. These regions can be filled with free electrons or dust consisting of “astronomical silicate” and graphite. A photon works its way through the model region and generally undergoes several scattering processes. The emission directions, path lengths between scattering events and the scattering angles are given by Monte Carlo routines based on classical intensity distributions (section 3.1). During each scattering event the Stokes vector is changed by multiplication with the corresponding Mueller matrix (section 3.2). For dust scattering, absorption is important and a large fraction of the photons never reaches the virtual observer. The relevant cross sections and matrix elements for dust scattering and extinction are computed on the basis of Mie theory applied to distributions of spherical graphite and silicate grains (section 3.3).

If a photon escapes from the model region it will be registered by a web of detectors arranged in a spherical geometry around the AGN. The flux and polarization information of each detector is obtained by adding up the Stokes parameters of all detected photons. If the model is completely axially symmetric these can be azimuthally added and, if there is plane symmetry, the top and bottom halves are added. The AGN can be looked at in total flux, in polarized flux, percentage of polarization and the position angle at each viewing angle.

3.1. The Monte Carlo method and the basic routines of STOKES

Using the Monte Carlo method it is possible to generate a random event x according to a given probability density distribution $p(x)$. Let $p(x)$ be defined on the interval $[0, x_{max}]$. Then we can construct the probability distribution function $P(x)$ and relate it to a random number r between 0 and 1 as follows:

$$r = P(x) = \frac{1}{C}\int_0^x p(x')dx'. \quad (1)$$

The constant C is a normalization constant resulting from integration over the whole definition interval $[0, x_{max}]$. It thus keeps the values of $P(x)$ between 0 and 1. Given the random number r the according value x for a single event is obtained by inverting (1). A fairly detailed explanation of the Monte Carlo method can be found in Cashwell & Everett (1959). In the following, we describe the main routines of *STOKES* and denote all randon number computed from equation (1) by r_i, with $i = 1, 2, 3....$

3.1.1. The *source* routine

A variety of continuum, broad-line region, and narrow-line region geometries are available in *STOKES*: cylindrical, toroidal, spherical, and double-conical source regions can be defined. To generate a model photon its initial parameters position, flight direction, and wavelength have to be set. Assuming a constant density of the emitting material a random position for the new emitted photon will be sampled. The flight direction is given by two angles, θ and ϕ, in a standard polar coordinate system centered on the photon’s position. Assuming isotropic emission we have the following sampling equations for the angles:

$$\theta = \arccos(1 - 2r_1), \quad (2)$$

$$\phi = 2\pi r_2. \quad (3)$$

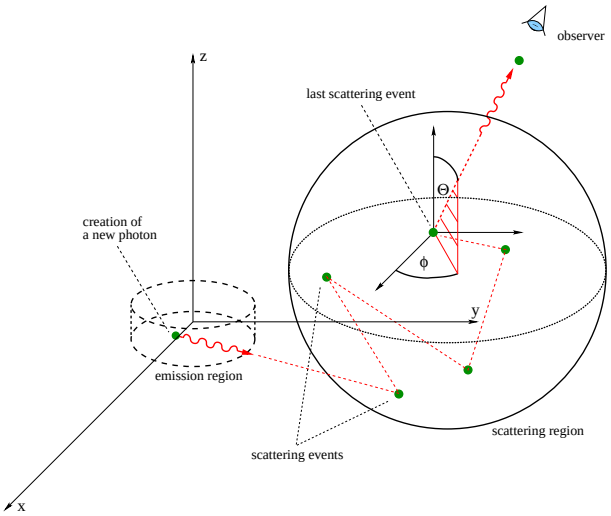

Fig. 1. A photon working its way through the model space.

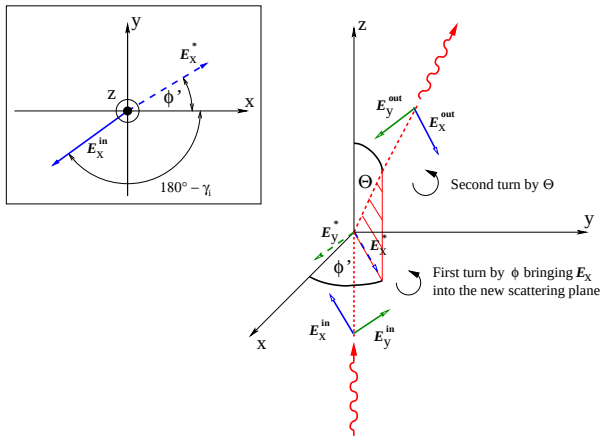

Fig. 2. Geometry and denotations for a single scattering event. The inset shows the first rotation of the ***E***-vector by the angle ϕ, the view on the polarization plane is along the negative z-axis.

The wavelength of the photon is sampled according to the intensity spectrum over a range $[\lambda_{min}, \lambda_{max}]$. We have the sampling equations

$$\lambda = \begin{cases} \left[\lambda_{min}^{\alpha} + r_3\left(\lambda_{max}^{\alpha} - \lambda_{min}^{\alpha}\right)\right]^{\frac{1}{\alpha}}, & \alpha \neq 1, \\ \lambda_{min}^{\alpha}\left(\frac{\lambda_{max}^{\alpha}}{\lambda_{min}^{\alpha}}\right)^{r_3}, & \alpha = 1. \end{cases} \tag{4}$$

The value α denotes the usual power law index of the intensity spectrum. Note that the above sampling equation automatically takes care of the wavelength-dependence of photon energy.

3.1.2. The *proceed* routine

If we ignore scatterings back into the beam, the intensity of a photon beam traversing a slab of scattering material with particle number density N and cross-section σ will drop by a factor of $e^{N\sigma l}$, with l being the distance traveled inside the scattering region. From this one can derive the sampling function of l:

$$l = \frac{1}{N\sigma}\ln(1 - r_4). \tag{5}$$

The factor $\frac{1}{N\sigma}$ is the mean free path length. Depending on the scattering material, the program will use either a dust extinction cross-section σ_{ext} computed from Mie theory or, in case of electron scattering, the Thomson cross section σ_{Th}.

3.1.3. The scattering routines

Consider a photon being scattered off a spherical particle (see Fig. 2). The outgoing electromagnetic wave associated with the photon can be resolved into two components (see e.g., Bohren & Huffman, 1983). These components refer to directions of the electric-field vector parallel and perpendicular to the scattering plane. We name the two components $E_{\parallel}$ and $E_{\perp}$. For scattering off a spherical particle the following relation between the incoming and scattered electric fields holds:

$$\begin{pmatrix} E_{\parallel,s} \\ E_{\perp,s} \end{pmatrix} = \begin{pmatrix} S_2(\theta) & 0 \\ 0 & S_1(\theta) \end{pmatrix} \begin{pmatrix} E_{\parallel,i} \\ E_{\perp,i} \end{pmatrix}. \tag{6}$$

The values $S_1(\theta)$ and $S_2(\theta)$ are the so-called scattering matrix elements. They are independent of the azimuthal angle ϕ. In case of Thomson scattering they are given by simple analytic expressions:

$$S_1(\theta) = \cos^2\theta, \tag{7}$$
$$S_1(\theta) = 1. \tag{8}$$

For dust scattering the albedo and the matrix elements of a standard dust grain are calculated from Mie theory (see section 3.3). The albedo at the photon wavelength is compared to a random number r_5 in order to decide whether the photon is absorbed or scattered. In case of absorption, the photon is lost, and the cycle starts over with the generation of a new photon by the *source routine*.

If the photon is scattered the angle-dependent classical intensity distribution of a scattered electromagnetic wave measures the probability of finding it at a certain direction. Such probability density distributions are derived from equation (6).

In order to also consider the impact of the incident polarization on the scattering angle, we split up the incident intensity I_i into a completely polarized and a completely unpolarized part:

$$I_i = I_{i,pol} + I_{i,unpol} = P_i I_i + (1 - P_i)I_i. \tag{9}$$

The incident polarization is denoted by P_i, its position angle by γ_i. Both are calculated from the incident Stokes parameters of the photon. We now rotate the polarization plane around the incident flight direction by the angle $180° - \gamma_i$ in

order to reach a position where the incident electric-field vector of the completely polarized component is aligned with the reference axis (position angle = 0° from the *x*-axis, see the inlet of Fig. 2). We then compute the angle-dependent intensity I_s behind the scattering center from equation 6 together with equation 9:

$$I_s(\theta,\phi') = \frac{I_i}{k^2 d^2}\left[\begin{array}{c} \frac{1}{2}\left(|S_1(\theta)|^2 + |S_2(\theta)|^2\right)(1-P_i)+ \\ \left(|S_1(\theta)|^2 \sin^2\phi' + |S_2(\theta)|^2 \cos^2\phi'\right) P_i \end{array}\right], \quad (10)$$

with d being the distance between the scattered photon and the scattering center, and k denoting the wave-number. Considering this intensity as a probability density p, we obtain the probability distribution for the scattering angles θ and ϕ':

$$P(\theta) = N \int_0^{\pi} \left(|S_1(\theta)|^2 + |S_2(\theta)|^2\right) \sin(\theta') d\theta', \quad (11)$$

$$P_\theta(\phi') = \frac{1}{2\pi}\left(\phi' - \frac{|S_1(\theta)|^2 - |S_2(\theta)|^2}{|S_1(\theta)|^2 + |S_2(\theta)|^2} P \frac{\sin 2\phi'}{2}\right). \quad (12)$$

The number N is a normalization constant in order to make (11) range from 0 to 1 for scattering angles between 0° and 180°. To sample ϕ' and θ, the right hand-sides of these equations have to be set equal to random numbers r_6, r_7. Then, they are solved for the angles. Note that the sampling of the scattering angle θ is independent of the incident polarization. Since at the beginning we performed a coordinate transformation to make the electric-field vector oscillate along the reference axis, the sampling of ϕ' has to be followed by the back-transformation

$$\phi = 180^\circ - \gamma_i + \phi'. \quad (13)$$

This procedure of finding the sampling equations for the scattering angles is analogous to the one followed by 1994.

3.2. Polarization formalism and scattering

The Stokes vector of each photon lies perpendicular to its direction of flight and is defined relative to a co-moving coordinate system inside the polarization plane. We assume newly created photons coming from the source are unpolarized. Hence, their Stokes vectors have the very simple form:

$$\begin{pmatrix} I \\ Q \\ U \\ V \end{pmatrix} = \begin{pmatrix} 1 \\ 0 \\ 0 \\ 0 \end{pmatrix}. \quad (14)$$

With each scattering event, the co-moving coordinate system undergoes a double rotation: the first rotation, by the azimuthal angle ϕ, happens around the current flight direction of the photon. It rotates the **E**-vector inside the polarization plane to the position of the new scattering plane (see Fig. 2). Physically, it does not affect the polarization state, but the Stokes vector undergoes the following coordinate transformation (1983):

$$\begin{pmatrix} I^* \\ Q^* \\ U^* \\ V^* \end{pmatrix} = \begin{pmatrix} 1 & 0 & 0 & 0 \\ 0 & \cos 2\phi & \sin 2\phi & 0 \\ 0 & -\sin 2\phi & \cos 2\phi & 0 \\ 0 & 0 & 0 & 1 \end{pmatrix} \begin{pmatrix} I^{in} \\ Q^{in} \\ U^{in} \\ V^{in} \end{pmatrix}. \quad (15)$$

The second rotation happens inside the scattering plane and by the scattering angle θ. The change of the Stokes vector is determined by the so-called Mueller matrix. For scattering off a spherical particle, the matrix is of the following form:

$$\begin{pmatrix} I^{out} \\ Q^{out} \\ U^{out} \\ V^{out} \end{pmatrix} = \frac{1}{k^2 d^2} \begin{pmatrix} S_{11} & S_{12} & 0 & 0 \\ S_{12} & S_{22} & 0 & 0 \\ 0 & 0 & S_{33} & S_{34} \\ 0 & 0 & -S_{34} & S_{44} \end{pmatrix} \begin{pmatrix} I^* \\ Q^* \\ U^* \\ V^* \end{pmatrix}. \quad (16)$$

The entries of the Mueller matrix are closely related to the elements of the scattering matrix $S_1(\theta)$ and $S_2(\theta)$ as is explained in section 3.3

When a photon is recorded by one of the virtual detectors, it is necessary to rotate the polarization plane around the flight direction until it matches with the reference axis of the detector. Then, the Stokes vectors of all incoming photons can be added up to the values $\hat{I}$, $\hat{Q}$, $\hat{U}$ and $\hat{V}$. Finally, the net polarization properties are derived from:

$$P = \frac{\sqrt{\hat{Q}^2 + \hat{U}^2 + \hat{V}^2}}{\hat{I}}, \quad (17)$$

$$\gamma = \frac{1}{2} \arctan \frac{\hat{U}}{\hat{Q}}. \quad (18)$$

3.3. Computation of Dust properties

Mathis, Rumpl, & Nordsieck (1977) suggested dust compositions to reproduce extinction curves observed in our Galaxy. They assumed spherical dust grains having a size distribution proportional to a^s, with a being the grain radius and s a given index. Weingartner & Draine (2001) further developed the model by using carbonaceous and siliceous dust compositions to verify interstellar extinction in the Milky Way and in the Magellanic clouds. The dust compositions that can be modelled with *STOKES* are based on this work. The user can choose the minimum and maximum radii of the grain size distribution, its index s, and the abundances of graphite and silicate.

The Mie data, i.e. scattering and extinction cross sections, albedo, and entries of the scattering matrix, are computed using the code given by Bohren & Huffman (1983). We imported complex dielectric functions for graphite and silicate measured by Draine & Lee (1984). For graphite, two dielectric functions have to be considered since the optical properties for light polarized parallel and perpendicular to the crystals axis differ from each other. The program therefore works with two

different kinds of graphite having abundances in a ratio of 1:2.

The code computes a weighted average of the dust composition and grain size distribution defined. The properties of the resulting "standard dust grain" are used by the *proceed* and the *scattering* routines of *STOKES*.

4. Simulation of torus geometries

In the present paper we confine ourselves to using *STOKES* to investigate the continuum polarization expected for AGNs if the main elements of the current standard unification scheme are correct. We want to investigate general constraints on the geometry of quasars by modelling their polarization, although none of our models are intended to reproduce observational polarimetric data for any specific object. Our main goals are to be able to reproduce the observed degree of polarization in both type-1 and type-2 Seyferts and in particular to be able to explain the type-1/type-2 relative polarization position angle dichotomy. We also confine ourselves to using standard Galactic dust such as is seen in the solar neighborhood, even though there is evidence that the grains in the tori and AGNs might be somewhat larger and depleted in carbonaceous grains (see Gaskell et al. 2004, 2005).

As discussed in section 1, there is good observational evidence both for the existence of a dusty, optically-thick torus surrounding the central black hole and the putative accretion disc, and, at least in some objects, for scattering cones along the polar axis. The difference in polarization between the NLR and BLR generally places the scattering region outside the BLR, but inside the NLR (e.g., Angel et al. 1976). The polarization produced by simple scattering cones is quite straightforward. They produce polarization perpendicular to the radio axis, as is commonly observed in type-2 AGNs but they cannot produce the parallel polarization seen in type-1 AGNs. Polarization by the torus itself is considerably more complicated. In the following we concentrate firstly on trying to see how much of the polarization properties of type-1 and type-2 AGNs can be produced by a uniform-density torus *alone*. In particular we will show that scattering off a torus alone can *not* explain the type-1/type-2 dichotomy.

Kartje (1995) modelled the AGN polarization induced by scattering off a cylindrical torus. This torus model was adopted from the fit to NGC 1068 given by Pier & Krolik (1992). The torus is geometrically rather compact, situated within a radius of only 1 pc around the central source. Such a torus is not necessarily physical, so we investigate whether the results of Kartje can be confirmed with more general tori, and we extend the range of parameter space explored.

4.1. Curved surfaces versus sharp edges

The progress made in the previous studies reviewed in section 2 is gratifying. In the following sections we expand the variety of simulated AGN geometries. The tori examined by Wolf & Henning (1999), Kartje (1995), Young (2000), and Watanabe et al. (2003) have rather sharp edges, and since we find that polarization results can depend strongly on geometric details, we have investigated a less artificial torus geometry with an elliptical cross-section. To examine the influence of sharp edges of the Kartje torus on the polarization we define a torus with similar dimensions, similar optical depth of 750 along the radius in the equatorial plane, but having an elliptical cross-section (see Fig.3).

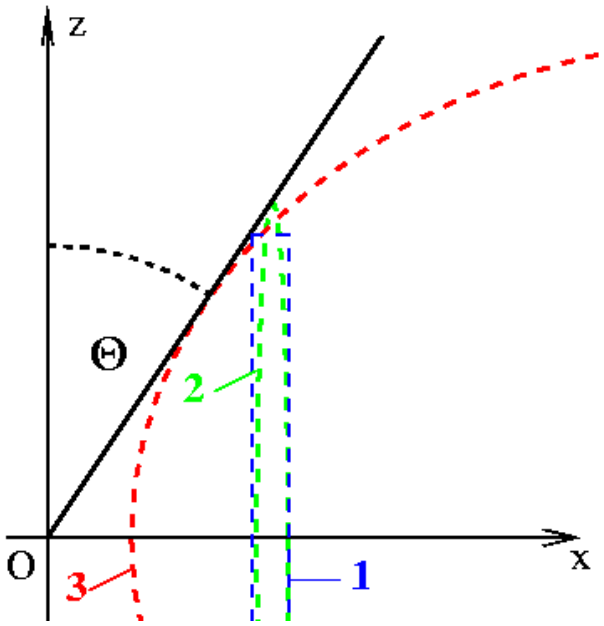

Fig. 3. Geometry of the three torus models we consider: (1) the cylindrical torus used by Kartje., (2) a compact elliptically-shaped torus, and (3) an extended elliptical torus. All tori have the same half-opening angle Θ_0

Our results compare very well to those obtained by Kartje (1995). In Fig.4 we show polarization and flux (normalized to the flux of the central source) versus wavelength at different viewing directions. The torus considered has a half-opening angle of $\theta_0 = 30$ deg. The figure is quite similar to the corresponding diagrams in Kartje's paper (see his Fig.5). In our simulations the torus was filled with standard Galactic dust, following the prescription of Mathis, Rumpl, & Nordsieck (1977). We sampled a total 4×10^8 photons and recorded spectra at 10 different viewing angles scaled in $\cos i$ where i is measured from the axis of the torus. This scale of $\cos i$ represents an equal angular flux distribution for an isotropic source at the center of the model space.

The only difference between our results and those of Kartje is that we generally obtain slightly lower polarization degrees and a slightly different wavelength-dependent slope for the scattered flux. Also, the minimum in the polarization is shifted to shorter wavelengths. This can be explained by the fact that we calculated our cross-sections from Mie theory of a specific dust composition whilst Kartje used cross-sections given by Mathis, Mezger, & Panagia (1982).

We also investigated the polarization for changing θ_0 and again obtained similar results (not shown) to those for Kartje's cylindrically-shaped tori. Thus, our first result is that the differences in polarization between the elliptical and cylindrical tori

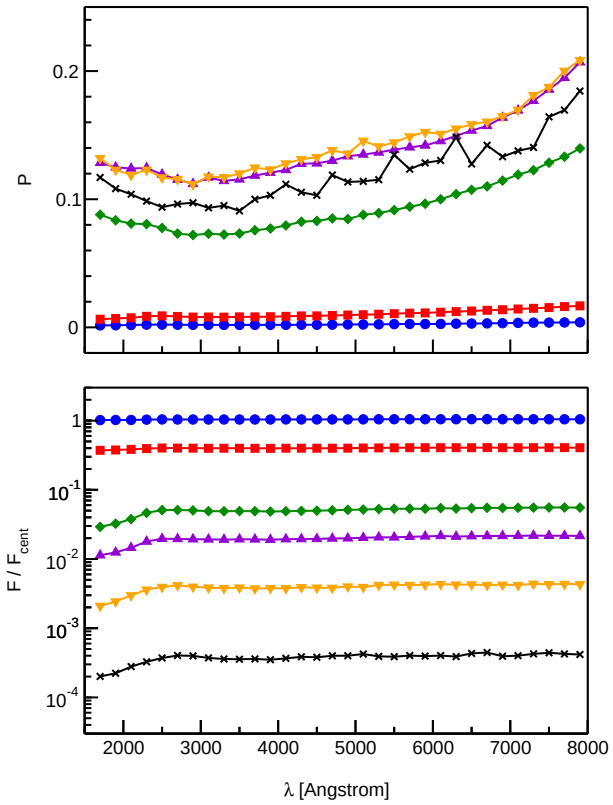

Fig. 4. Modeling a Kartje torus with an elliptical cross-section (see section 4.1). Top: polarization, P. Bottom:the fraction, F/F_*, of the central flux, F_*, seen at different viewing inclinations, i. Legend: $i = 87°$ (= edge-on) (black crosses), $i = 76°$ (orange triangles with points down), $i = 57°$ (purple triangles with points up), $i = 41°$ (green diamonds), $i = 32°$ (red squares), and $i = 18°$ (= face-on) (blue circles).

are negligible. So having sharp edges in the cylindrical model rather than the more realistic rounded edges of the elliptical torus does not introduce spurious effects.

4.2. The effect of the shape of the inner edge of the torus

A real torus is undoubtably thicker than the geometrically thin cylindrical torus of Kartje. Direct imaging of NGC 4261 (= 3C 270) shows that the dusty torus in that AGN extends out to 230 pc (Ferrarese, Ford, & Jaffe, W. 1996). A similar dust lane across the nucleus of M 51 (= NGC 5194) extends ~ 100 pc (Ford et al. 1992). The inner radii of tori are given by infra-red reverberation mapping of the hot dust and are ~ hundreds of light-days (Glass 2004).

The outer regions of tori have considerable optical depth so their precise shape is unimportant since no photons escape parallel to the equatorial plane of the torus. The shape of the inner region facing the central energy source is more important. Current torus models commonly consider curved inner surfaces. We thus model optically-thick, uniform-density tori with elliptical cross sections, an inner radius of 0.25 pc, and an outer radius of 100 pc. The half-opening angle, θ_0, will be an important parameter for the obscuration and reflection properties, and we examine half-opening angles ranging from 10° to 75°. Variation of θ_0 is realized by changing the vertical half-axis of the elliptical torus cross section. We determine the dust density by fixing the visual optical depth τ_V along the equatorial plane of the torus at again 750. Thus, practically no photon is able to penetrate through the torus and only scattering off its surface is relevant.

Variability implies that the size of the optical and UV-continuum source is less than a few light-days, as is also expected from simple black-body emissivity arguments. Hence, when considering scattering off the torus, we can neglect the finite size of the continuum source in our model and assume a point-like emission region.

If the viewing angle, i, is less than θ_0 corresponding to a type-1 object, we only observe a regular type-1 spectrum. We find that there is no significant polarization in this case. If we look at a type-2 object at a higher inclination angle (Fig.5) we only detect scattered and hence polarized light.

There are differences between our results of modeling a large torus (case 3) with half-opening angle $\theta_0 = 30$ deg and compare it to a smaller torus (case 2) with identical half-opening angle but smaller dimensions – see Fig.4. We show the differences in the P and the fraction of the light making it to the observer, as a function of viewing angle in Fig.6. A striking difference occurs in the angular flux distribution. The large torus will scatter considerably fewer photons towards an observer at intermediate viewing angles. At $i \sim 63$ deg, for instance, the flux difference in the V-band is of a factor of 35. At edge-on viewing angles the probability of seeing scattered photons is much lower than for the small dimensional torus of similar θ_0.

There are also some difference in the polarization signature of both tori. Although the overall spectral dependence of P is the same, the level of P has changed at some viewing angles. The strongest change is at higher inclinations, toward an edge-on view when the central source is becoming obscured by the torus view. For the larger torus P is significantly higher at these viewing directions. This difference is also found for higher i.

The difference between a compact and the expanded torus can be understood by considering the geometry of both tori (see Fig.7). There are three main differences. The first is that whilst having the same half-opening angle, the large torus offers a smoother cutoff of the emission cone. Photons leaving the central region along the arrows in Fig.7 are thus still likely to be absorbed by the large torus but escape from the compact torus. Thus from type-2 viewing positions one sees more of the inside of the torus where scattered photons originate. The second factor is that photons scattered off the large torus at edge-on viewing angles are more likely to be the result of multiple scattering, and these photons will reduce the net polarization. The third difference is that in the smaller torus case the observer is seeing the opposite inside wall of the torus so that photons are scattered at a less forward-scattering angle (i.e., the angle of scattering is closer to 90°.). Because of the phase function for scattering this results in greater polarization of the scattered light. The lower polarization arising from the larger

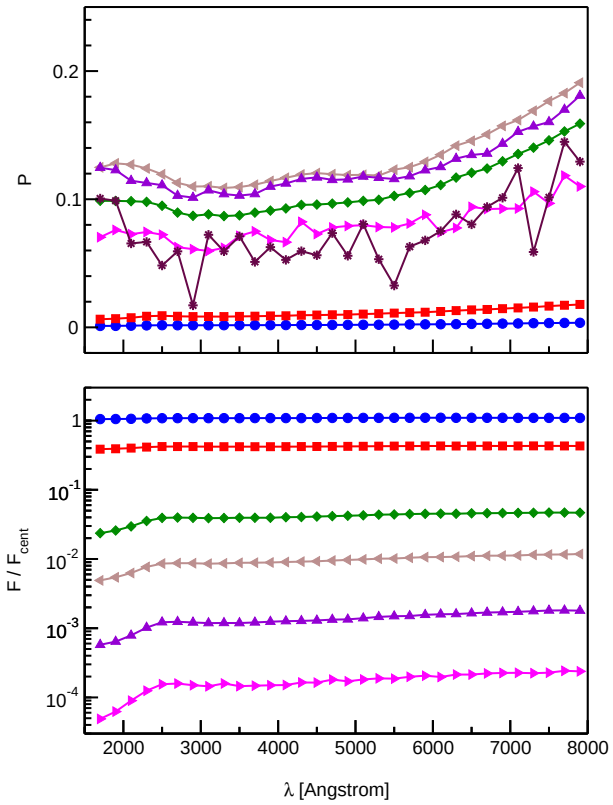

Fig. 5. Modelling a large torus with an elliptical cross-section (see section 4.2). Top: polarization, P. Bottom: the fraction, F/F_*, of the central flux, F_*, seen at different viewing inclinations, i. Legend: $i = 70°$ (=intermediate) (maroon stars), $i = 63°$ (pink triangles with points to the right), $i = 57°$ (purple triangles with points up), $i = 49°$ (tan triangles with points to left left), $i = 41°$ (green diamonds), $i = 32°$ (red squares), and $i = 18°$ (=face-on) (blue circles)

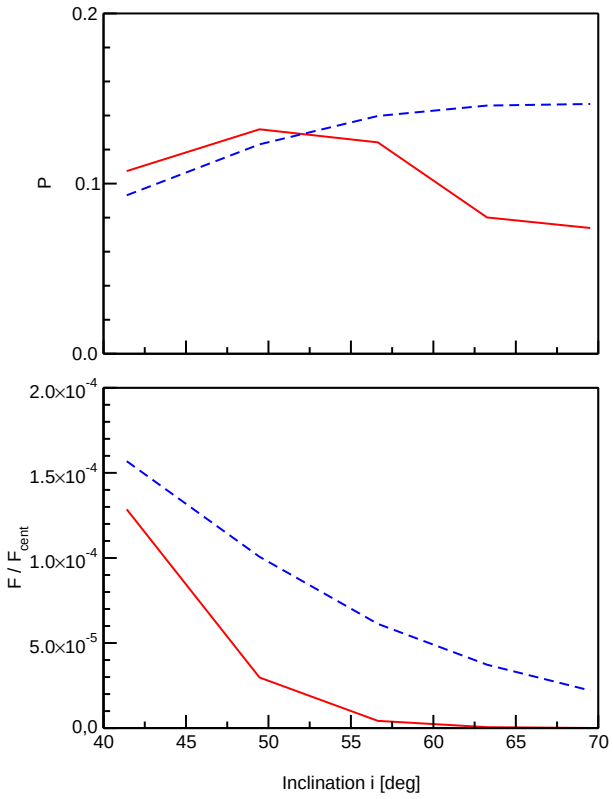

Fig. 6. Differences between large and small tori. Modelling a large torus with an elliptical cross-section (see section 4.2). Top: polarization, P, and bottom, the fraction, F/F_*, of the central flux, F_*, as a function of viewing inclinations, i. The dashed lines denote the thin elliptical torus (case 2), the solid line the extended torus (case 3)

torus is thus a result of seeing less of the inside of the torus, having more depolarizing multiple scatterings, and and having less favorable scattering angles for polarization.

4.3. The effect of the torus opening angle

In our modelling of the large torus we find that θ_0 is a dominant parameter for both the degree, P, and position angle, γ, of polarization.

In Fig.8 we show the wavelength-dependent polarization of the scattered radiation for various half-opening angles, θ_0, of the torus. We have averaged the polarization over all type-2 viewing angles, i.e., all directions with $i > \theta_0$ where the source is being covered by the optically-thick torus and hence the observer is only seeing scattered radiation. For viewing angles, i, with $i < \theta_0$ corresponding to a type-1 object seen face-on, the polarization is negligible.

In order to illustrate more clearly the general effect of the opening angle on the polarization, we plot the effective polarization P_{eff} as a function of the half-opening angle of the torus in Fig.9. The effective polarization is obtained by averaging P over the considered wavelength range and over different viewing angles. Since the polarization for type-1 viewing angles is negligible, we only show the averages over $i > \theta_0$.

Varying the opening angle shows two important things. Firstly, the polarization decreases as the opening angle increases (see Fig.9). For $\theta_0 \approx 60°$ the torus polarizes least effectively. The second important result is that the *angle of polarization* also varies with the half-opening angle θ_0. For θ_0 significantly smaller than 60° the position angle favors a direction perpendicular to the symmetry axis, as is observed in type-2 AGN, whereas when θ_0 becomes larger than 60°, the direction of the $\boldsymbol{E}$-vector switches to being oriented parallel to the axis of symmetry (see Fig.8). The reason for the flip of relative position angle can be explained by the the assymmetric scattering phase function and by the geometry of the inner parts of the torus (Kartje 1995). For a distant observer looking at the torus along an off-axis line of sight, the scattered radiation comes from the inner surface walls. These consist of the inner torus wall facing most directly the observer on the one hand side, and of the two surfaces on the side on the other. Due to the scattering geometry the photons scattered off the side walls are polarized along the projected symmetry axis, whilst the photons coming from the far wall are perpendicularly polarized.

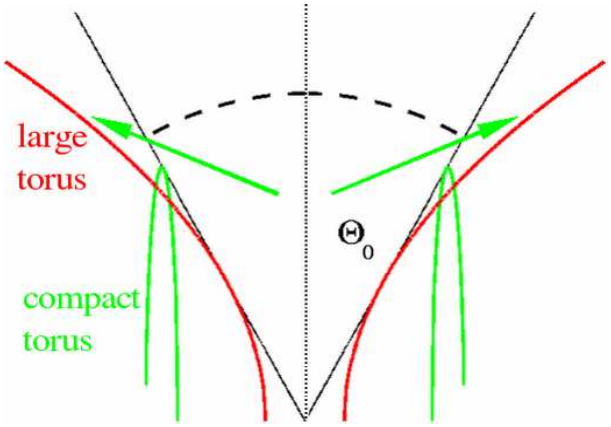

Fig. 7. Comparison of the compact and the extended torus having the same opening angle θ_0. The extended torus blocks more effectively the photons being scattered toward type-2 viewing directions.

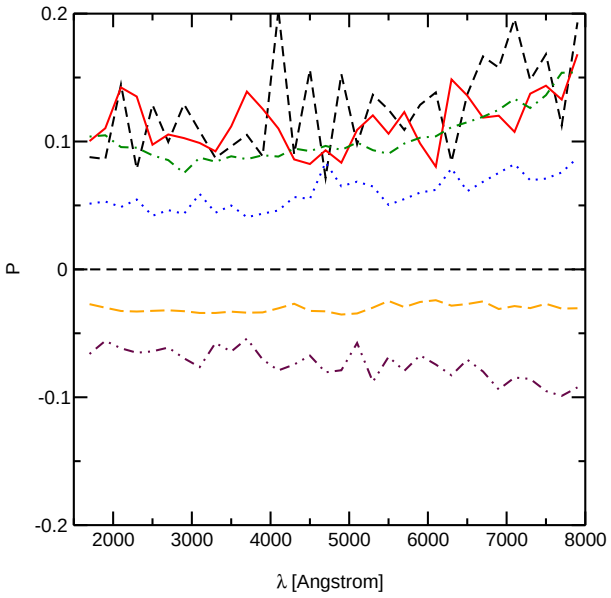

Fig. 8. Polarization averaged over all type-2 viewing angles (see text). A positive value of polarization denotes an ***E***-vector oriented perpendicular to the torus symmetry axis, for negative values the ***E***-vector is aligned with the projected axis. Legend: Θ = 10° (black dashed line), Θ = 20°(solid red line), Θ = 30°(green dot-dashed line), Θ = 45°(blue dots), Θ = 60°(long yellow dashes), and Θ = 75°(purple double dots and dashes)

The ratio of the so-defined inner surfaces change with the half-opening angle of the torus, and so does the overall polarizatioin vector. It follows that a scattering disc produces polarization with the ***E***-vector parallel to the axis of symmetry. This direction of polarization is the opposite of what is observed in type-2 AGNs.

Our results therefore show that both the observed degree of polarization and its relative position angle thus *require tori with small opening angles*. In particular, tori with half-opening angles greater than 60° are excluded.

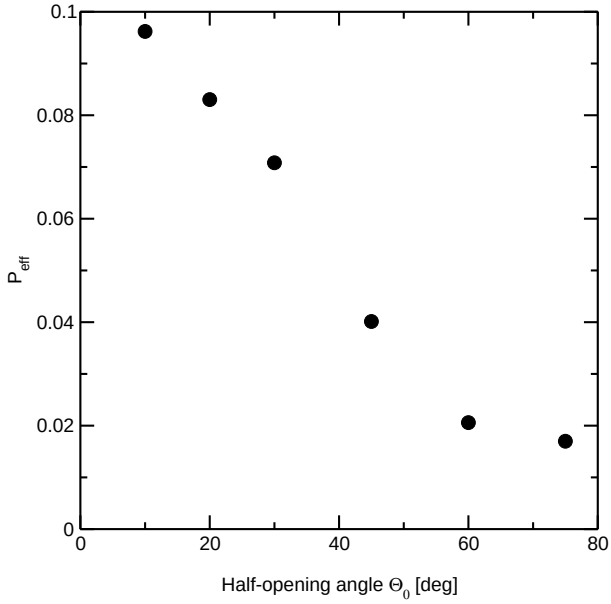

Fig. 9. Effective polarization P_{eff} (see text) for edge-on (type-2) viewing positions as a function of the half-opening angle for an extended torus (case3).

4.4. Wavelength insensitivity of polarization due to dust scattering

Inspection of the wavelength-dependent polarization curves for the geometries considered above shows that the polarization for all the viewing angles and half-opening angles we have considered is almost wavelength-independent over the optical and the UV. This is surprising at first sight, since, as is well known the scattering cross section of interstellar grains increases strongly from the optical to the UV and in the past wavelength-independent polarization has been considered to be the fingerprint of Thomson scattering off of electrons.

Our apparently contradictory result arises because we are dealing with scattering off optically-thick material and because of the relatively small variation of the albedo over the optical and UV spectral regions. The relative constancy of the albedo means that the average scattering and extinction cross sections vary almost in the same way and the probability of destruction of a photon because of absorption varies only slightly with wavelength. Since we are dealing with an optically-thick torus we see emergent photons that have been scattered at an optical depth $\tau \sim 1$. This is regardless of wavelength [1]. The increase in scattering cross-section with decreasing wavelength only means that the shorter wavelength photons we see have been scattered closer to the surface of the torus. A significant change in albedo with wavelength, however, will cause a color dependency in the intensity and polarization of the scattered

[1] This is the reason that the sunlit sides of clouds in the earth's atmosphere are extremely white.

light[2]. As Zubko & Laor (2000) point out, the wavelength dependence of polarization provides a probe of the grain scattering properties.

Another grain property that theoretically needs to be considered is the degree of asymmetry of the scattering since this is effectively an angle-dependent albedo change. At short wavelengths dust is strongly forward scattering and this will give an increase in polarization with decreasing wavelength in forward-scattered directions (see the left-hand side of Fig. 7 of Zubko & Laor 2000). This is unimportant for our models since almost none of the photons the observer sees are forward scattered.

5. The type-1/type-2 dichotomy

Stockman, Angel, & Miley (Stockman et al.(1979)) made the seminal discovery that, for low-polarization, high-optical-luminosity, radio-loud AGNs, the optical polarization position angles tend to align *parallel* to the large-scale radio structure. Since synchroton radiation is intrinsically polarized in the direction of the magnetic field and hence in the direction of the jet, they speculated that the parallel alignment could be the result of seeing some synchrotron emission in the optical. They also suggested polarization from an optically-thin, non-spherically symmetric scattering region near the source of optical radiation as another possibility.

Antonucci (1982) made another interesting discovery that whilst many radio galaxies showed a similar parallel alignment of the polarization and radio axes, there was, unexpectedly, a population showing a *perpendicular* relationship. This made a synchrotron origin for the polarization much less likely, but perpendicular polarization, as we have shown above, is easy to produce with scattering.

Antonucci subsequently showed that relatively-radio-quite Seyfert galaxies show a similar dichotomy between the predominantly but not exclusively parallel polarization in face-on type-1 Seyferts and the perpendicular polarization of type-2 Seyferts.

As we have shown in section 4, producing the perpendicular polarization of type-2 AGNs is straight forward. The problem in modeling the type-1/type-2 polarization dichotomy is the production of polarization vectors *parallel* to the symmetry axis of the torus once one rejects a synchrotron origin. We have seen in the previous sections that a dusty torus can only produce polarization vectors oriented perpendicular to this axis except for the case of extremely-thin tori which are inconsistent with the observations. Also polar electron cones, that have previous been assumed in some unified scheme of AGNs, will not solve this problem because they produce perpendicular polarization.

We have already noted in section 4 that an extremely flat dust distribution can produce parallel polarization. Tori cannot have such a flat distributions for at least two reasons: they are incompatible with the ratios of type-1 and type-2 objects, and very flat distributions have too low covering factors to produce the reprocessed IR emission. This leads us to explore the important suggestion of Goodrich & Miller 1994 that the parallel polarization of type-1 objects arises from scattering in a flattened electron-scattering medium (see also Young 2000, Smith et al. 2004, and Smith et al. 2005).

The energy in an AGN is widely believed to originate in an accretion disc. Such a disc has a flattened geometry, and at the temperatures needed ($\sim 10^5$K), electron scattering will be the dominant opacity. This ionized material offers a geometrical shape similar to the oblate spheroids modelled by Angel (1969). Angel has shown that an optically-thin uniformly emitting cloud of electrons will produce polarization parallel to the cloud's minor axis.

In this section we investigate disc-like emission and scattering regions of various geometries and optical depths and observe the resulting polarization properties at different inclination angles. We consider both uniformly-emitting regions such as could correspond to the inner accretion disc itself, and centrally-illuminated flattened distributions that could correspond to flattened ionized outflows from the AGN. For all models we quote vertical electron-scattering optical depths, τ_{es}, measured outwards from the center of the equatorial plane perpendicular to the disc (i.e., parallel to the axis of symmetry).

We first consider uniform-density, emitting and scattering disks of 1 light-day in diameter d and vary the height h to define different ratios $\frac{h}{d}$. We consider a "thick disc" of cylindrical cross section with $\frac{h}{d} = 0.5$ (see Fig.10) and a "thin disc" with $\frac{h}{d} = 0.02$ (see Fig.11). The optical depth is varied by adjusting the electron density. We investigate τ_{es} between 0.001 and 50.

For the case of a geometrically-thick emitting disc (see Fig. 10) we obtain at most moderate polarization values of a few percent. The degree of polarization depends strongly on the viewing direction and the optical depth. For lower optical depth the $\boldsymbol{E}$-vector is aligned with the disc's symmetry axis. It flips to a perpendicular orientation for $\tau_e s$ greater ~ 15.

This behaviour is also seen for the spheroidal models of Angel (1969). The polarization goes through a maximum at $\tau_{es} \sim 3$ at an edge-on viewing direction. Note that such an edge-on view angle will not be seen for type-1 objects, however, since this direction is blocked by the torus. In type-1 objects one is probably mostly viewing at inclination angles of $\sim 30^\circ$ or less so the polarization will not exceed $\sim 1\%$.

Much stronger values of the polarization can be obtained when the disc is flatter. For the geometrically-thin disc we have a similar qualitative behaviour as for the thick disc (compare Fig. 11 with Fig. 10), but the degree of polarization reaches higher values and is significant even for near to face-on viewing directions. The flip to perpendicular (type-2) polarization occurs at a moderate optical depth ($\tau_{es} \sim 4$) and at an edge-on viewing angle that cannot be seen for type-1 objects. A thin disc with moderate optical depth will thus produce parallel polarization for all type-1 viewing positions.

The polarization behaviour of our uniformly emitting discs can be explained in the same manner as the behaviour of the polarization of the oblate spheroids of Angel (1969). For low τ_{es} the net polarization is mainly determined by the photons travelling parallel to the disc plane and then being scattered toward the surface and further-on to the observer. For an observer, who

[2] This is the cause of colorations in the atmosphere of the giant planets.

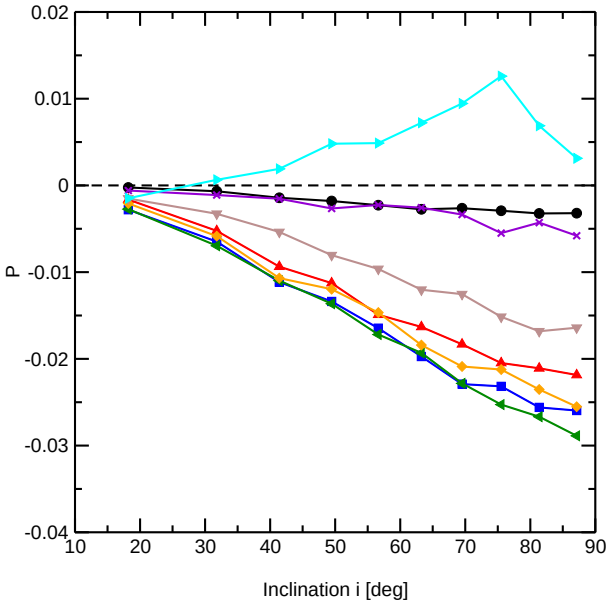

Fig. 10. Polarization versus viewing angle for a geometrically-thick emitting and scattering electron disc with $\frac{h}{d}$ = 0.5. The different curves denote various vertical optical depths for the disc. Positive polarization values stand for polarization position angles perpendicular to the disc's symmetry axis, for negative values the polarization vector is aligned with this direction. Legend: τ_{es} = 0.025 (black circles), τ_{es} = 0.25 (red triangles with points up), τ_{es} = 0.5 (blue squares), τ_{es} = 0.75 (green triangles with points left), τ_{es} = 1.25 (orange diamonds), τ_{es} = 2.5 (brown triangles with points down), τ_{es} = 12.5 (purple crosses), τ_{es} = 50 (cyan triangles with points right).

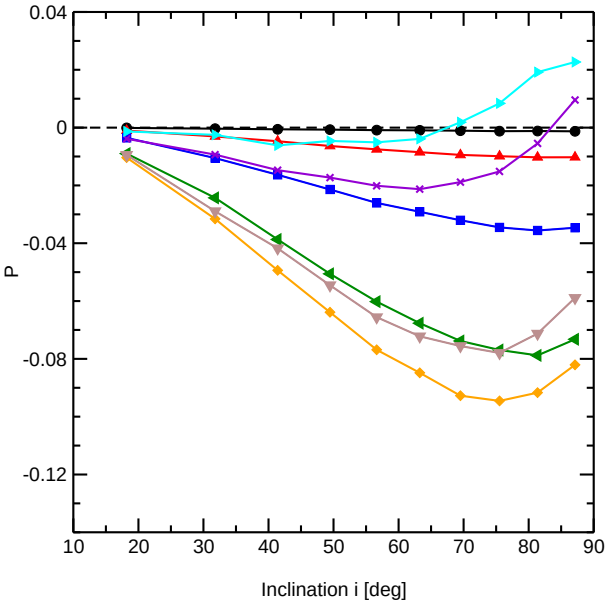

Fig. 11. Same parameters as in Fig.10, but for a thin disc with $\frac{h}{d}$ = 0.02. Legend: τ_{es} = 0.001 (black circles), τ_{es} = 0.01 (red triangles with points up), τ_{es} = 0.05 (blue squares), τ_{es} = 0.2 (green triangles with points left), τ_{es} = 0.5 (orange diamonds), τ_{es} = 1 (brown triangles with points down), τ_{es} = 3 (purple crosses), τ_{es} = 5 (cyan triangles with points right).

does not observe the disc exactly face-on, the integrated scattered flux from the disc surface will be polarized along the projected direction of the disc axis. This can be understood by the fact, that polarization by electron scattering is most efficient for orthogonal scattering angles. For the same reason, the polarization is strongest at edge-on viewing angles.

When the optical depth becomes higher, multiple scattering of photons travelling toward the disc surface becomes relevant. The polarization vector induced by the last scattering event before leaving the disc will preferably by oriented perpendicular to the disc axis. Hence, the polarization position angle flips and on the way to this transition P becomes very low.

For clarity we show in Fig. 12 the dependence of the polarization at a maximum type-1 viewing position of $i \sim 30°$ as a function of τ_{es}. Here, we are modeling a very thin emitting electron disk with a geometrical ratio of $\sim$ 0.0005, which is compariable to the dimensions of an accretion disk in AGN. As can be seen, for modeling of a uniform-density accretion disk the highest polarizations are obtained for low optical depths. The highest parallel polarization is achieved for $\tau_{es} \sim 0.5$ and polarizations in the observed range ($P \sim 1\%$, Antonucci 1982, 1983) can even be obtained with $\tau_{es} \sim 0.1$

In Fig. 13 we consider the effect of the geometry of the electron-scattering region by examining the following shapes: (1) A uniform emitting and scattering disc, similar to those in Figs. 10, 11, and 12, with various ratios of height to diameter; (2) a flat scattering torus illuminated by a central point source; (3) two types of centrally-illuminated, electron-scattering cylinders. The shapes (2) and (3) could correspond to an electron-scattering region such as an atmosphere or flattened outflowing wind above the outer cooler parts of a disc as previously discussed by Young et al. (1999), Young (2000) and Smith et al. (2004). We consider cases where this external electron-scattering region covers the central source, and where there is a hole in the middle. In all four cases τ_{es} = 1, and as in Fig. 12 we are looking at the object at a maximal type-1 viewing position.

It can be seen in Fig. 13 that except for the thinnest distributions (the left-hand side of the figure) there is a similar dependence of P on the relative thickness. Chaning the geometrical shape of the scattering disk shifts the overall level of polarization but the dependence on the geometrical ratio largly remains the same. The slight difference between the uniformly-emitting disc and the external scattering discs is that in the latter case the photons all begin in the middle of the plane, while in the former case some of the photons originate near the surface and so see an lower optical depth.

For the thinnest scattering regions there is a major difference between those that cover the central point source and those that have a hole in the center. When the region with the hole is very thin the covering factor of the central source is low, few photons are scattered, and therefore the polarization must be low.

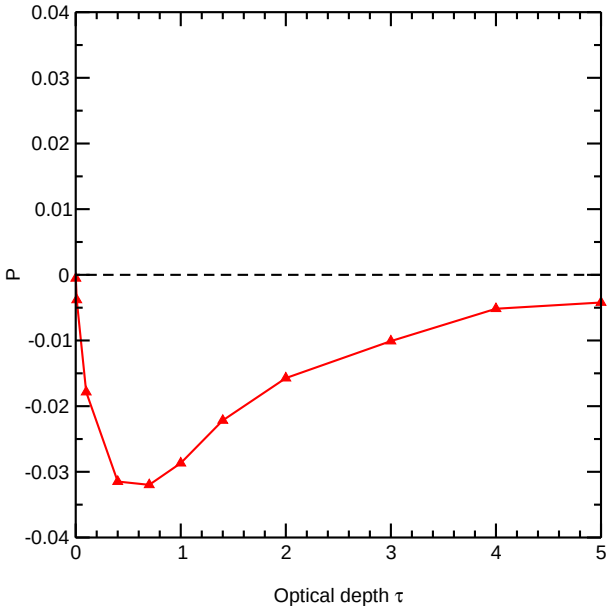

Fig. 12. The effect of the vertical optical depth, τ_{es}, on the polarization of a very thin disc observed from the maximal type-1 viewing angle. The negative polarization denotes polarization parallel to the axis of symmetry.

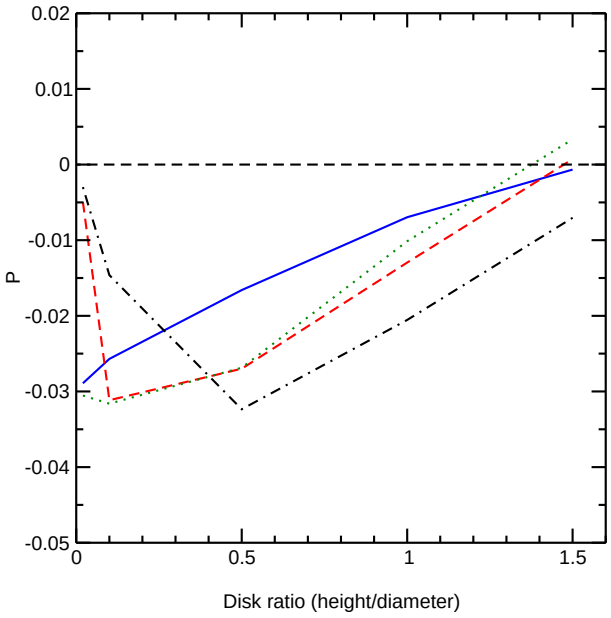

Fig. 13. The effect of the flatness of the electron scattering region on polarization for four different geometries viewed from the maximal type-1 viewing position. Legend: Emitting and scattering disc (blue solid line), flat scattering torus (black dot-dashed line) illuminated from the center, scattering cylindrical disc with inner and outer radii in the ratio 2:7 illuminated from the center (dashed red line), scattering disc with very narrow funnel covering a point source (dotted green line). A negative polarization denotes polarization parallel to the axis of symmetry.

We only consider the possibility of electron scattering close to the black hole and not dust scattering for several reasons. Firstly, dust will not survive this close to the central continuum source. IR reverberation mapping puts the inner edge of the dusty torus just outside the broad-line region in agreement with the predicted sublimation temperature. If we replace the electrons in the models discussed in this section with dust it does not give a high enough polarization (less than around 1% even for highly-inclined viewing positions and around 0.1% at best for more likely near face-on, type-1 viewing angles) because the dust is forward scattering. Because there is absorption for dust grains the number of photons coming out is also lower than in the electron-scattering case.

6. Discussion

6.1. Wavelength-independent polarization from dust scattering off an optically thick torus

Modeling a uniform-density torus we obtain observed polarization values for type-2 objects of a few percent without considering polar dust or electron scattering. Furthermore, the wavelength dependence of polarization is rather similar for different geometrical shapes of the inner torus surface: a flat surface (case 1), as was shown by Kartje (1995), a slightly curved shape (case 2), or a convex shape (case 3) all reveal a nearly flat polarization spectrum over the optical and UV range. From polarimetric oservations it is thus not immediatley obvious to deduce the geometry of dust distributions in AGN close to the nucleus.

The lack of wavelength-dependent polarization we find is important for interpreting spectropolarimetry of type-2 AGNs. Wavelength-independent polarization is observed in the nuclei of type-2 AGNs such as NGC 1068 (Antonucci & Miller, 1985) IRAS 09104+4109 (Hines & Wills, 1993). Because of the wavelength independence of the polarization close to the nucleus of NGC 1068, Miller, Goodrich, & Mathews (1991) interpret this as electron scattering in an outflowing polar wind. They have difficulties however in maintaining the ionization of the outflow and require an intrinsically anisotropic continuum to ionize the outflow. We propose instead that the wavelength independent polarization arises from the walls of the torus. On the other hand, Miller, Goodrich, & Mathews observe strongly wavelength-dependent polarization from a cloud near the nucleus. The reason that this shows rising polarization to shorter wavelengths must be because it is optically thin, as would indeed be expected for an interstellar cloud in such a position or gas associated with the NLR.

6.2. Equatorial scattering disks

For type-1 objects scattering off dust in the polar regions of the object only has a small impact on the observed polarization because the scattering angle is relativly small. Our modeling shows that polarization induced by a dusty torus is also very low along type-1 viewing angles. It is hence necessary to introduce additional structures to the unified scheme to explain type-1 polarization. We confirm that at type-1 viewing angles polar-

ization can be produced by scattering off an equatorial disk as was suggested by Smith et al. (2002). The rotating BLR disk they introduce together with the surrounding co-planar scattering region reproduces very well the turnover of the polarization vector observed in the Hα and Hβ lines of many objects.

Following this idea a little further, we presume that the highly ionized accretion disk should have a similar effect for the polarization of the optical and UV continuum. The difference to an externally irradiated equatorial scattering disk is that the emitting and scattering material are intermixed. We show in Fig.13 that the dependence on the geometry of the emitter (flat versus thick) is similar for emitting disks and for centrally irradiated scattering discs, however, the polarization degree obtained by an extended emitter is somewhat lower. This is caused by the fact that a significant fraction of the photons is produced close to the surface and thus unlikly to undergo scattering events. They dilute the polarization of the photons coming from deeper inside the disk.

The over all picture of type-1 one polarization properties become more complicated by introducing additional scattering regions. It is widely believed that the transformation of gravitational energy into radiation happens by an accretion disk and hence its contribution to the continuum polarization can not be neglected. Making the simplified assumption that all type-1 polariazation of the continuum comes from the accretion disk we can obtain a range of the electron densitiy neccessary to reproduce the observed polarization precentage. From Fig. 12 we derive that observed values of a few percent for the type-1 polarization require an Thomson optical depth between 0.1% and 4%. Our modeling shows that this corresponds to an electron density of 1.5×10^{10} cm^{-3} —6×10^{11} cm^{-3}.

6.3. Polarization properties of AGN in the unifed scheme

OUr implified overall prediction for the polarization behaviour of a typical AGN is summarized in Fig. 14 where we show the polarization behavior for an idealized AGN consisting of an electron scattering accretion disc surrounded by a dusty torus as it is viewed from various angles.

We have found that the polarization is somewhat higher for a smaller steeper torus (see Fig. 6) than for a larger more gradual one. A real torus probably has a steep inside to it. This is because the dust radius is set by dust sublimation and so will be determined primarily by the inverse square of the distance from the central source. Thus the inside of the torus is probably concave as seen from the central source. The source creates a spherical region, with radius of the order of the sublimations radius of the dust grains, around the center where the dust composition is likely to be very different to the dust farther away. Destruction of small dust grains will modify the grain size distribution and hence the albedo and scattering properties are likely to change. It is an interesting future task to model polarization by scattering off a dusty torus using dust compositions different from the Galactic composition we adopted here.

If scattering off the torus produces the polarization in type-2 AGN, then our results suggest that the majority of AGN have

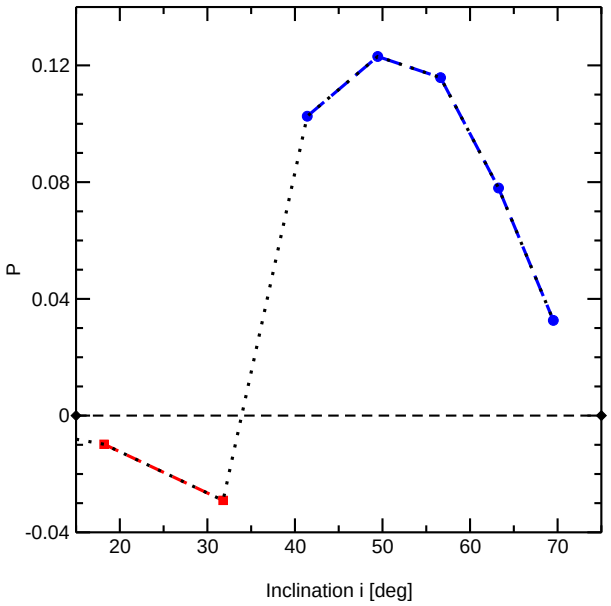

Fig. 14. Dependence of polarization on viewing angle of a typical AGN. The model shows the V-band polarization resulting from a thin accretion disc of geometrical ratio 50000:1 and $\tau es = 1$) and a torus with a 30° half-opening angle. A negative polarization denotes polarization parallel to the axis of symmetry.

narrow openings. Wide opening angles produce parallel polarization in type-2 AGN, which is not observed. However, this torus polarization could be overwhelmed by polarization from any scattering material located above the disk.

There is good evidence that the fraction of type-2 AGNs decreases with luminosity, declining from ~ 80% when log L = 42 to ~ 30% when $logL$ = 46. In the standard unified model such a change corresponds to the opening angle increasing with luminosity. Since we show that the polarization from the torus is a function of opening angle (see Fig. 9), we predict that, on average, the polarization of type-2 AGNs will increase with luminosity.

A larger opening angle of the torus corresponds to a smaller covering factor of the central source with dust. One measure of the opening angle is the relative IR flux since it depends on the dust covering factor. We therefore predict that the degree of polarization should be correlated with the relative strength of th thermal IR flux.

Observations of the polarization of the broad lines will give important constraints on the geometry of polarizers close to the central engine in type-1 AGNs and we plan to pursue further modelling of this. If the polarization of the continuum is arising from the accretion disc itself then the BLR will show a different polarization. If the polarization is arising in a flattened wind outside the BLR then both the continuum and the BLR can show similar polarization; there is evidence that this is indeed the case (Smith et al. 2002).

Since the scale of the BLR is similar to the scale of the flattened electron-scattering region and not much smaller than

the scale of the dust-scattering regions, at least slight differences in polarization are to be expected between the lines and the continuum and also across line profiles, especially if there is asymmetry present in the distribution of the scatterers or the line-emitting material. Temporal polarization variability on a BLR crossing timescale is also possible. Since all these things are observed there are interesting things to explore in future work.

Since the polarization of both type-1 and type-2 AGNs depends on viewing angle, we predict that the polarization properties will depend on orientation indicators such as the radio properties, the width of Hβ, and the presence of various types of intrinsic abgsorption-line systems.

7. Conclusions

We have developed a versatile Monte Carlo code for modelling polarization produced by scattering in many astrophysical situations. We have shown that it reproduces previous results well.

Modelling polarization with a uniform-density torus for different half-opening angles we have reproduced the observed range of polarization (0% to 20%) over the optical and the UV using scattering off the torus alone. There is no need to invoke electron-scattering cones.

Polarization observations of type-AGNs favor tori with small half-opening angles ($\sim 60\tilde{\text{deg}}$) since the polarization of type-2 AGNs decreases with the opening angle of the torus. Large opening angles are ruled out because for half-opening angles greater than $\sim 60°$ the polarization has the wrong relative position angle.

Since in the standard unified model the opening angle increases with luminosity, we predict that, on average, the polarization of type-2 AGNs will decrease with luminosity.

The spectral shape of the polarization produced by scattering off of a torus is nearly wavelength-independent. The nuclear scattering in NGC 1068 is probably produced by dust in the torus and not by electron cones. This removes the difficulty of having to maintain the degree of ionization of the putative electron cones.

The polarization behaviour is not strongly sensitive to details of the torus geometry (e.g., cylinders with sharp edges, versus tori with smooth elliptical cross-sections).

Our modelling shows that scattering by the torus alone cannot explain the polarization dichotomy between type-1 and type-2 AGNs since the degree of polarization for type-1 objects is negligible in all our modelled cases. This result is not changed by adding scattering cones of electrons since they produce polarization at the wrong angle. For type-1 AGNs the polarization must be associated with other processes closer to the central engine.

The parallel polarization seen in type-1 AGNs arises naturally from electron scattering for a wide range of flattened distribution close to the central energy source. As well as the flattened external equatorial electron scattering region proposed by Goodrich & Miller (1994), polarization will arise in the accretion disc itself. At a given viewing angle the polarization of the different types of region does not depend strongly on the geometry of the electron-scattering region, but it is a strong function of optical depth. A relatively low optical depth of only a few tenths can produce the observed polarization.

Acknowledgements. We are grateful to the University of Nebraska Computer Science department for providing access to the University of Nebraska's *Prairiefire* supercomputer. David Swanson and Mako Furukawa provided valuable assistance in transfering the code to *Prairiefire*. We wish to thank Ski Antonucci and Mark Bottorff for helpful conversations about the structure of AGNs, and Tim Gay and Paul Finkler for useful discussions of the atomic physics background of various scattering phenomena. RWG thanks the Department of Physics and Astronomy of the University of Nebraska for their hospitality.

This research has been supported by the Hans-Böckler-Stiftung in Germany.

References

Angel, J. R. P. 1969, ApJ, 158, 219
Angel, J. R. P., Stockman, Woolf etc???
Antonucci, R. R. J, 1982, Nature, 299, 605
Antonucci, R. R. J, 1983, Nature, 303, 158
Antonucci, R. R. J., 1993, ARA&A, 31, 473
Antonucci, R. R. J., 2002, in Astrophysical spectropolarimetry, ed. J. Trujillo-Bueno, F. Moreno-Insertis, & F. Snchez (Cambridge, UK: Cambridge University Press), 151
Antonucci, R. R. J., & Miller, J. S., 1985, ApJ, 297, 621
Baker, J. C., & Hunstead, R. W., 1995, ApJ, 452, L95
Bohren, C. F., & Huffman, D. R., 1983, in "Absorption and Scattering of Light by Small Particles", Wiley, New York
Cashwell, E. D., & Everett, C. J., 1959, in "Monte Carlo Methods for Random-Walk Problems", Pergamon Press
De Zotti, G. & Gaskell C. M. 1985, A&A, 147, 1
Draine, B. T., & Lee, H. M. 1984, ApJ, 285, 89
Efstathiou, A., & Rowan-Robinson, M., 1995 MNRAS, 273, 649
Ferrarese, L., Ford, H. C., & Jaffe, W.1996, ApJ, 470, 444
Fischer, O., Henning, Th., & Yorke, H. W.1994, A&A, 284, 187
Ford, H. C., Caganoff, S., Kriss, G. A., Tsvetanov, Z., & Evans, I. N. 1992, BAAS, 24, 818
Gaskell, C. M., Benker, A. J., & Antonucci, R. R. J., 2005, in preparation.
Gaskell, C. M., Goosmann, R. W., Antonucci, R. R. J., & Whysong, D., 2004, ApJ, 616, 147
Glass, I. S. MNRAS, 350, 1049
Goodrich, R. W. & Miller, J. S. (1994), ApJ, 434, 82
Gordon, K. D., Misselt, K. A., Witt, A. N., & Clayton, G. C., 2001, ApJ, 551, 269
Hall, J. S. 1949, Science, 109, 166
Hiltner, W. A. 1949, ApJ, 109, 471
Hines, D. C., Schmidt, G. D., Gordon, K. D., Smith, P. S., Wills, B. J., Allen, R. G., Sitko, M. L., 2001, ApJ, 563, 512
Hines, D C., Wills, B. J., 1993, ApJ, 415, 82
Hurt, T., Antonucci, R. R. J., Cohen R., Kinney A., & Krolik J. H., 1999, ApJ, 514, 579
Kartje, J. F., 1995, ApJ, 452, 565
Keel, W. C. 1980, AJ, 85, 198
Kishimoto, M., 1999, ApJ, 518, 676
Lawrence, A. & Elvis, M. 1982, ApJ, 256, 410
Martel, A., 1998, ApJ, 508, 657
Mathis, J. S., Rumpl, W., & Nordsieck, K. H., 1977, ApJ, 217, 425
Mezger, P. G., Mathis, J. S., & Panagia, N. 1982, A&A, 105, 372
Miller, J. S., Goodrich, R. W, & Mathews, W. G. 1991, ApJ, 378, 47

Misselt, K. A., Gordon, K. D., Clayton, G. C., & Wolff, M. J., 2001, ApJ, 551, 277
Pier, E. A. & Krolik, J. H. 1992, ApJ, 401, 99
Rowan-Robinson, M. 1977, ApJ, 213, 635
Smith, J. E., Young, S., Robinson, A., Corbett, E. A., Giannuzzo, M. E., Axon, D. J., & Hough, MNRAS, 2002, MNRAS, 335, 773
Smith, J. E., Robinson, A., Alexander, D. M., Young, S., Axon, D. J., Corbett, Elizabeth A. 2004, MNRAS, 350, 140
Smith, J. E., Robinson, A.,, Young, S., Axon, D. J., Corbett, Elizabeth A. 2004, MNRAS, 359, 846
Stockman, H. S., Angel, J. R. P., & Miley, G. K. 1979, ApJ, 227, L55
Tran, H. D., Brotherton, M. S., Stanford, S. A., van Breugel, W., Dey, A., Stern, D., & Antonucci, R. R. J., 1999, ApJ, 516, 85
Watanabe, M., Nagata, T., Sato, S., Nakaya, H., & Hough, J. H. 2003, ApJ, 591, 714
Weingartner J. C., & Draine B. T. 2001, ApJ, 548, 296
Wills, B. J. & Browne, I. W. A. 1982, ApJ302, 56
Wolf, S., & Henning, T., 1999, A&A, 341, 675
Wolf, S., Henning, T., & Stecklum, B. 1999, A&A, 349, 839
Young, S., 2000 MNRAS, 312, 567
, Corbett, E. A., Giannuzzo, M. E., Hough, J. H., Robinson, A., Bailey, J. A., & Axon, D. J. 1999, MNRAS, 303, 227
Young, S., Hough, J. H., Efstathiou, A., Wills, B. J., Bailey, J. A., Ward, M. J., Axon, D. J., 1996, MNRAS, 281, 1206
Young, S., Hough, J. H., Axon, D. J., Bailey, J. A., & Ward, M. J.1995 MNRAS, 272, 513
Zubko, V. G. & Laor, A. 2000, ApJS, 128, 245